applied sciences

MDPI

Article

Sedimentary Microfacies Analysis and Reservoir Prediction of Braided River Delta Reservoirs in Central Asia’s S Gas Field

Feilong Li [1,2,3,4], Yungui Xu [1,2,3,4,*], Haotong Liu [5], Youheng Leng [6], Zhanjun Wei [6], Nini Zhang [7], Ronghe Liu [6], Boyong Liao [7] and Xuri Huang [1,2,3,4]

[1] State Key Laboratory of Oil and Gas Reservoir Geology and Exploitation, Southwest Petroleum University, Chengdu 610500, China; lflsgmhxy1@163.com (F.L.)
[2] School of Geosciences and Technology, Southwest Petroleum University, Chengdu 610500, China
[3] Natural Gas Geology Key Laboratory of Sichuan Province, Southwest Petroleum University, Chengdu 610500, China
[4] Key Laboratory of Piedmont Zone Oil and Gas Geophysical Exploration Technology for Petroleum and Chemical Industry, Southwest Petroleum University, Chengdu 610500, China
[5] PetroChina Safety and Environmental Protection Technology Research Institute, No. 1, Huanghe Street, Changping District, Beijing 102206, China
[6] PetroChina International (Turkmenistan) Amu Darya Gas Company, No. 27, Chengfang Street, Xicheng District, Beijing 100032, China
[7] Geological Exploration and Development Research Institute of CNPC Chuanqing Drilling Engineering Company, Chengdu 610051, China
* Correspondence: yungui.xu@swpu.edu.cn

Featured Application

The integrated core–log–seismic workflow developed in this study is directly applicable to lithologic trap screening and well placement in deep Jurassic clastic gas reservoirs of the Amu Darya Right Bank, where conventional seismic interpretation alone is insufficient to resolve thin, heterogeneous channel sands.

Abstract

The prediction of thin-bedded, favorable sand bodies within the Middle-Lower Jurassic braided river delta–lacustrine succession of Block S (Amu Darya Right Bank) is challenging because of strong spatial heterogeneity, deep burial, and limited seismic resolution near the acoustic basement. To address this, we propose an integrated workflow that combines sedimentological characterization with geologically constrained seismic inversion. The study uses core, grain-size data, wireline logs, and 3D seismic surveys. Core–log–seismic integration first delineates three subfacies and nine numbered microfacies (MF1–MF9), with the delta front dominated by underwater distributary channels (MF1), mouth bars (MF2), and interdistributary bays (MF3). Planar microfacies distribution maps and electrofacies boundaries are then used as geological constraints for reservoir prediction. Steerable pyramid enhancement ($K = 4$ scales, $N = 6$ orientations) improves channel-reflection continuity, and PDF-regularized stochastic optimization inversion ($\lambda = 0.8$) is performed to identify thin sand reservoirs. Sand-ratio and GR cutoffs were validated against 412 core–log contacts in five wells. Discretization sensitivity tests confirm stable inversion under 2 ms and 4 ms sampling. The results show that (1) favorable Type I and Type II reservoirs occur preferentially in MF1 and MF2 (average porosities of 12.7% and 10.1%, respectively); (2) vertically, two sand-rich progradational intervals (Lower Member and late Upper Member) are separated by a transgressive mud-prone middle–early Upper Member; and (3) inversion low-impedance anomalies delineate strip-like and lobate channel–mouth-bar sand belts with thickness up to 14 m, consistent with well control. Fault-controlled graben–horst paleotopography influenced sand fairway distribution. The workflow highlights

Check for updates

Academic Editor: Keyu Liu

Received: 28 May 2026
Revised: 22 June 2026
Accepted: 22 June 2026
Published: 30 June 2026

https://doi.org/10.3390/app16136523

the value of integrating sedimentary microfacies boundaries as geological constraints in seismic inversion for heterogeneous deep clastic gas reservoirs.

Keywords: Amu Darya Right Bank; Middle-Lower Jurassic; braided river delta; sedimentary microfacies; steerable pyramid; stochastic seismic inversion; reservoir prediction

1. Introduction

Seismic sedimentology integrates seismic lithology and seismic geomorphology to reconstruct lithofacies, depositional systems, and basin evolution from 3D seismic data [1–3]. Recent workflows combining stratal slicing, attribute analysis, and geologically constrained inversion have improved the prediction of thin sand bodies in lacustrine delta systems, where conventional bandwidth limits vertical resolution [4–6]. Stochastic and PDF-regularized inversion further reduce uncertainty in data-limited settings by coupling well statistics with seismic amplitudes [7–13].

The Amu Darya Basin (∼420,000 km^2) is one of the largest superimposed hydrocarbon-bearing basins in Central Asia [14,15]. Its northeastern segment, the Amu Darya Right Bank, hosts major gas accumulations and remains an active exploration frontier owing to complex tectonics and multi-stage sedimentary fill [16–18]. Hydrocarbon production has historically targeted Upper Jurassic carbonate reef-shoal reservoirs [19–22]. Exploration is now shifting to the deeper Middle-Lower Jurassic clastic succession, which contains both reservoir-quality sandstones and coal-measure source rocks [23–25]. Regional studies document delta-front to littoral–shallow lacustrine associations and favorable source–reservoir–cap pairings [26], but block-scale microfacies architecture and geophysically constrained sand prediction remain limited.

Block S on the Kyzylkum Uplift exemplifies these gaps. Rapid facies change, fault compartmentalization, and strong heterogeneity coincide with deep burial and poor near-basement imaging [27]. Previous work in adjacent Central Asian basins emphasizes braided and deltaic sand-body complexity [28–30], yet Block S lacks a systematic microfacies scheme tied to reservoir ranking and inversion. Two issues are critical: (1) conventional seismic interpretation and inversion without robust facies control cannot resolve thin, channelized sands in deep clastic intervals; and (2) planar microfacies boundaries have not been used to constrain low-frequency models and inversion in this block, unlike recent fan-delta case studies that combine seismic sedimentology with waveform-indicative or statistically constrained inversion [3,31].

This study proposes an integrated workflow for the Middle-Lower Jurassic of Block S that parallels geologically constrained thin-sand prediction strategies in continental rift basins [3]: core–log–seismic microfacies characterization, planar facies mapping as geological constraints, steerable pyramid enhancement [32,33], and PDF-regularized stochastic optimization inversion [10,34]. Petrophysical ranking defines favorable facies belts, and inversion maps reservoir thickness for exploration targeting in deep Central Asian gas fields.

2. Geological Setting

The Amu Darya Basin lies in the southeastern Turan Plate and is bounded by the Western Tianshan Mountains (north), Kopetdag Mountains (south), Kyzylkum Mountains (west), and Afghanistan (east). The basin trends NW–SE and is structurally subdivided into the Central Karakum Uplift, Kopetdag Piedmont Depression, and North Amu Darya Depression, with NE- and NW-trending faults that controlled Mesozoic subsidence and sedimentation (Figure 1a). The Right Bank area comprises, from west to east, the Charzhu Uplift, Kyzylkum

Uplift, Karabeke Depression, Sandyktly Uplift, Beshkent Depression, and Gissar Piedmont Zone. Block S, the focus of this study, is situated on the Kyzylkum Uplift.

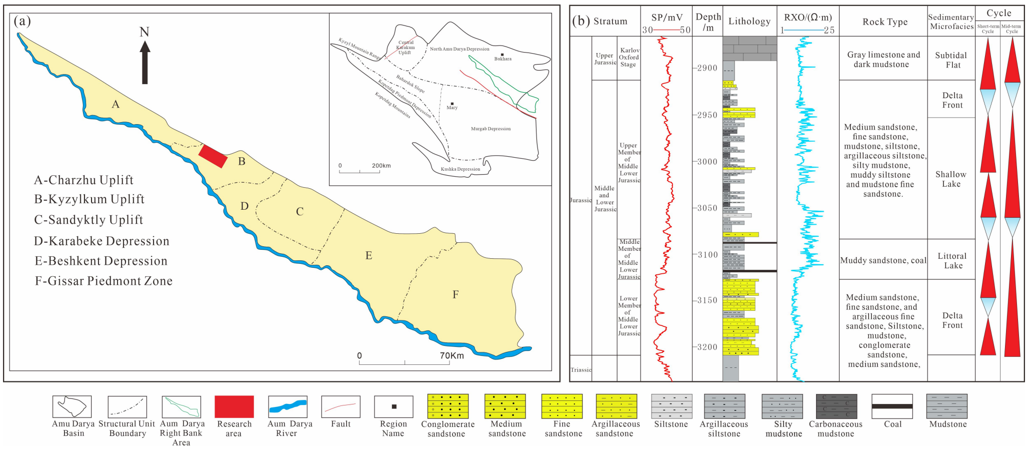

Figure 1. Tectonic framework of the Amu Darya Right Bank (**a**) and stratigraphic column of the Middle-Lower Jurassic in Block S (**b**).

Stratigraphically, the Right Bank succession includes a Paleozoic metamorphic basement, a Permian–Triassic transitional volcanic–clastic package, and a Jurassic–Paleogene sedimentary cover dominated by clastics, carbonates, evaporites, and coal seams. During Middle-Lower Jurassic deposition, the area experienced active rifting, producing a graben–horst paleotopography that favored development of large deltaic and lacustrine systems under abundant terrigenous supply [26,27]. NE- and NW-trending faults bound alternating structural highs (horsts) and lows (grabens); the northern Kyzylkum Uplift supplied coarse clastics into southern depocenters, locally controlling delta-front progradation and sand-body distribution (Figure 2). Based on lithology, wireline response, and cyclic stacking patterns, the Middle-Lower Jurassic in Block S is divided into Lower, Middle, and Upper members (Figure 1b).

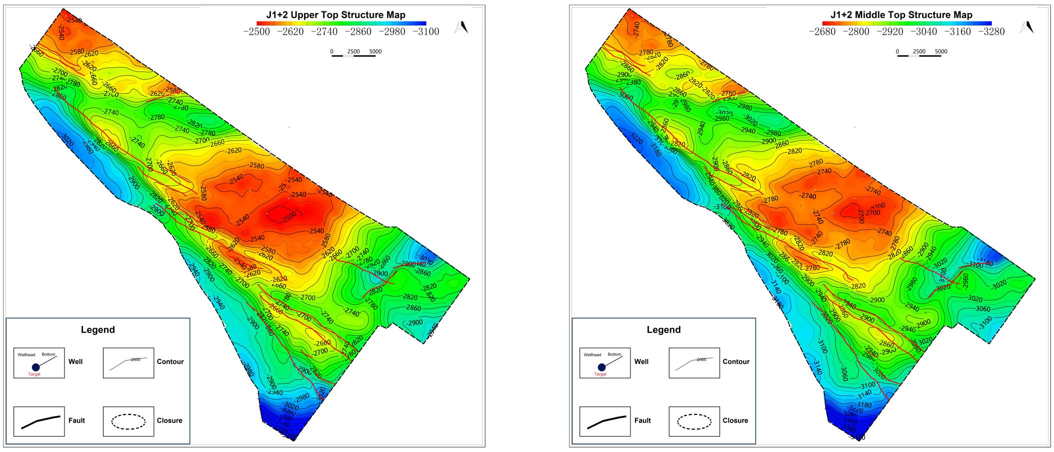

(**a**) (**b**)

Figure 2. *Cont.*

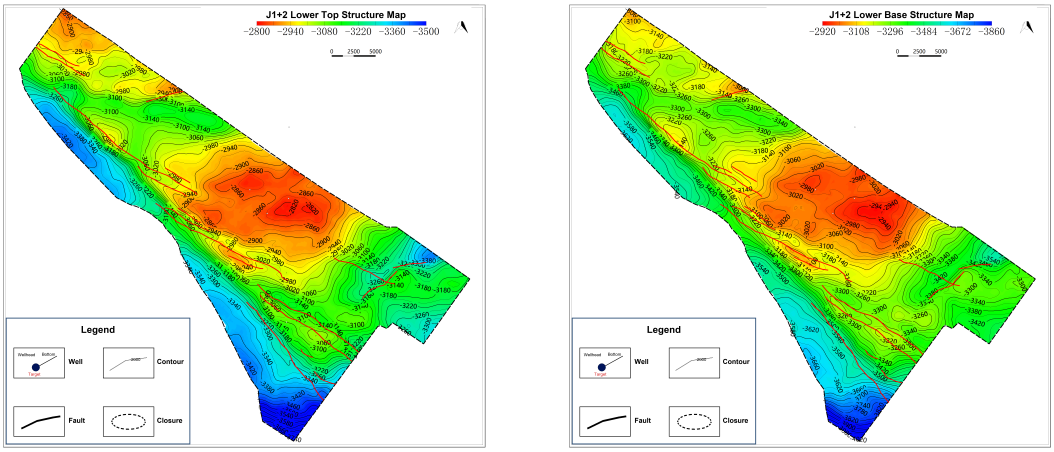

(**c**) (**d**)

Figure 2. Structure maps of the Middle-Lower Jurassic in Block S based on 3D seismic interpretation, illustrating fault-bounded graben–horst paleotopography at successive horizons: (**a**) Upper Member top; (**b**) Middle Member top; (**c**) Lower Member top; (**d**) Lower Member base (depth in m; faults in red).

3. Data and Methods

3.1. Dataset

The dataset comprises continuous core from five wells (S1, S2, G1, N2, and N5), wireline logs (gamma ray, SP, and deep resistivity) from four cored wells, 30 Middle-Lower Jurassic sandstone samples for sieve-based grain-size analysis, and a 3D seismic volume covering Block S (2 ms sample interval; dominant frequency ∼35 Hz). Core descriptions followed standard lithofacies coding based on grain size, sedimentary structures, and color. Logs were calibrated to core for electrofacies definition and stratigraphic correlation. Seismic data were tied at well locations; interpretation focused on reflection geometry, amplitude, and continuity in relation to log and core facies.

Reservoir cutoffs were derived from core–log cross-validation. At 0.5 m sampling intervals in the five cored wells, sand–mud contacts from core were compared with GR, SP, and resistivity curves. A GR threshold of 50 API separated sandy (GR $<$ 50 API) from muddy intervals with 87% agreement at bed boundaries ($n = 412$ contacts). Sand ratio (net sand thickness/total interval thickness) was computed for each 0.5 m window and correlated with core-derived porosity and permeability. Type I, Type II, and Type III facies belts correspond to sand ratios $>$0.4, 0.2–0.4, and $<$0.2, respectively, bracketing porosity thresholds of ∼8% and ∼5% and permeability thresholds of ∼2 mD and ∼0.5 mD (Table 1). These cutoffs are consistent with geologically constrained inversion practice in analogous deltaic systems [3,25].

Table 1. Classification and petrophysical characteristics of favorable reservoir facies belts in Block S. Sand-ratio cutoffs were calibrated from 0.5 m windows in five cored wells ($n = 412$) against porosity and permeability measurements.

Type	Microfacies	Sand Ratio	Avg. Porosity (%)	Avg. Permeability (mD)
Type I	MF1 underwater distributary channel	>0.4	12.7	8.3
Type II	MF2 mouth bar	0.2–0.4	10.1	4.7
Type III	MF5 beach bar	<0.2	4.5	1.6

3.2. Integrated Workflow

Following the strategy of coupling sedimentary facies mapping with constrained seismic inversion [1,3], the workflow comprised four steps (Figure 3):

(1) Sedimentary facies and microfacies characterization. Lithofacies, grain-size types, electrofacies, and seismic facies were identified from core, logs, and seismic profiles. Single-well columns and cross-well correlations resolved vertical stacking; planar microfacies maps were prepared for the Lower, Middle, and late Upper members.

(2) Geological constraints for reservoir prediction. Boundaries of underwater distributary channels, mouth bars, and interdistributary bays on planar microfacies maps were used as lateral guides for delineating sand-prone fairways, analogous to the use of facies belts and stratal boundaries to constrain low-frequency models in fan-delta inversion [3,11].

(3) Steerable pyramid seismic enhancement. Multi-scale, directionally filtered decomposition was applied to improve continuity and amplitude contrast of channel-related reflections prior to inversion [5,32,33].

(4) PDF-regularized stochastic optimization inversion. Well-derived acoustic-impedance (AI) PDFs regularized trace-wise inversion [9,10,34,35]. Inversion volumes were compared with GR-defined sands at wells and mapped for reservoir thickness.

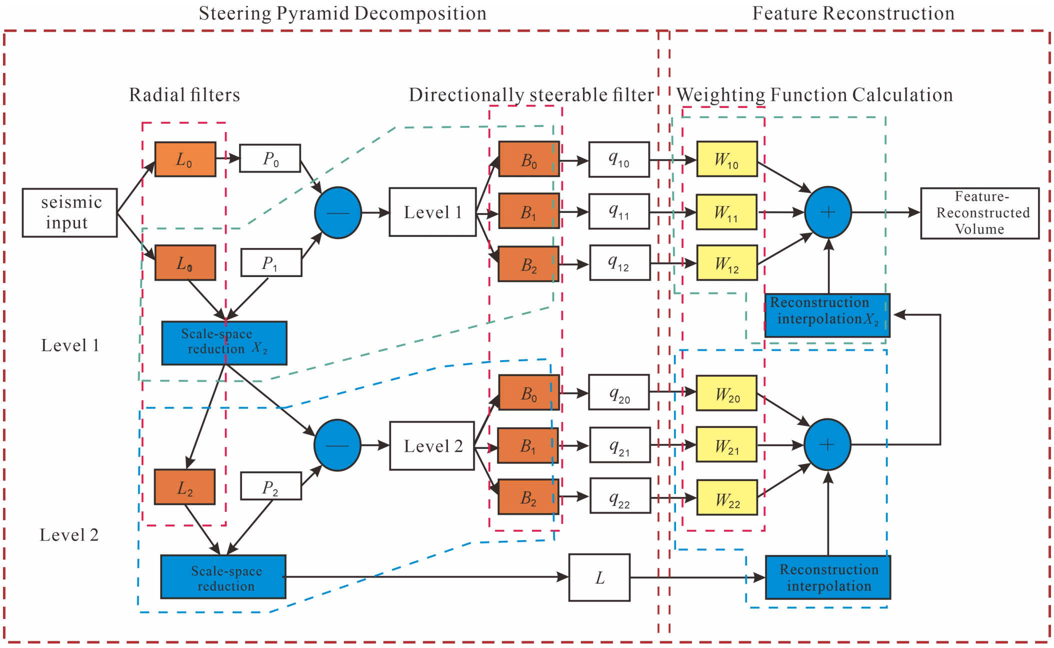

Figure 3. Workflow of steerable pyramid decomposition and feature reconstruction. Blue arrows indicate data flow; dashed boxes denote processing stages; colored panels show scale-wise filter responses.

3.3. Sedimentary Facies Analysis

Lithofacies were classified into sandstone, siltstone, and mudstone associations and further subdivided using standard sedimentary-structure codes (e.g., Sm, St, Fcl, Mm). Microfacies were identified by integrating lithofacies, electrofacies, and seismic facies, following a source-to-sink braided river delta–lacustrine facies model. Single-well facies columns and cross-well correlations were constructed to resolve vertical stacking patterns and lateral facies transitions. Planar microfacies distribution maps were prepared for the Lower, Middle, and late Upper members to capture progradational–retrogradational evolution. Petrophysical ranking of favorable facies belts combined core porosity and permeability measurements with casting thin-section observations.

3.4. Steerable Pyramid-Based Seismic Enhancement

Due to depth-related resolution loss and proximity to the acoustic basement, conventional seismic data poorly resolve thin channel sands. Steerable pyramid decomposition [32,33] was therefore applied to enhance channel-related reflections prior to inversion.

First, seismic data were decomposed into multiple scales in the frequency–wavenumber domain using radial filters:

$$S_k(x,y) = \mathcal{F}^{-1}\{H_k(f_x,f_y) \cdot \mathcal{F}\{S(x,y)\}\}, \tag{1}$$

where S_k represents the seismic component at scale k, and H_k denotes the radial bandpass filter.

According to steerable filter theory, a directional filter can be expressed as a linear combination of basis filters:

$$G_\theta(x,y) = \sum_{n=1}^{N} w_n(\theta) G_n(x,y), \tag{2}$$

where G_n are basis filters and $w_n(\theta)$ are orientation-dependent weighting functions.

Thus, the filtered seismic response at scale k along orientation θ is:

$$R_k(x,y,\theta) = S_k(x,y) * G_\theta(x,y). \tag{3}$$

Since the response is analytically continuous with respect to orientation, the optimal orientation at each spatial location is determined by maximizing the amplitude:

$$\theta^*(x,y) = \arg\max_\theta |R_k(x,y,\theta)|. \tag{4}$$

The corresponding optimal weighting function is denoted as $w_n(\theta^*)$ and the enhanced seismic data are reconstructed by combining the optimal responses across all scales (Figure 3).

In this study, the steerable pyramid was parameterized as follows to ensure reproducibility [32,33]: (i) $K = 4$ octave decomposition scales; (ii) $N = 6$ basis orientations per scale, sampled every 30° from 0° to 150°; and (iii) radial band-pass filters H_k with center frequencies of 10, 20, 40, and 80 Hz and bandwidths of one octave, applied to post-stack data with a 2 ms sample interval (Nyquist frequency 250 Hz). At each scale, the optimal orientation θ^* was estimated on a 5° grid, and the enhanced volume was obtained by weighted superposition of scale-wise responses.

This method improves the continuity and amplitude contrast of channel-related reflections (Figure 4).

The Middle-Lower Jurassic microfacies scheme used to bound inversion fairways comprises nine numbered types (MF1–MF9; Table 2).

Table 2. Numbered sedimentary microfacies of the Middle-Lower Jurassic in Block S.

No.	Code	Microfacies
1	MF1	Underwater distributary channel
2	MF2	Mouth bar
3	MF3	Interdistributary bay
4	MF4	Subaqueous natural levee
5	MF5	Beach bar
6	MF6	Littoral mud
7	MF7	Coastal swamp
8	MF8	Sand flat
9	MF9	Mud flat

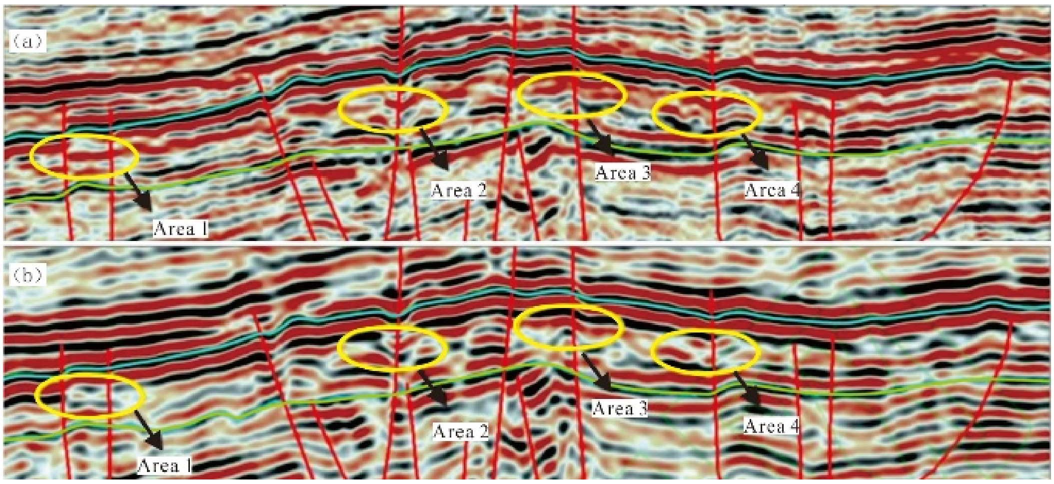

Figure 4. Comparison of seismic profiles before and after enhancement. Warm colors denote high amplitudes and cool colors low amplitudes. (**a**) Original seismic data; (**b**) enhanced seismic data.

3.5. Stochastic Optimization Seismic Inversion

Based on well-log analysis, AI values in the study area follow a stable statistical distribution. Rather than relying on variogram-based geostatistical inversion [7], we adopted a stochastic optimization scheme in which the well-derived AI PDF regularizes the inversion [9,10,34]. The overall workflow coupling geological constraints and well data is summarized in Figure 5.

3.5.1. Forward Model and Boundary Conditions

For a discretized impedance model $\mathbf{AI} = [AI_1, AI_2, \ldots, AI_M]^{\mathrm{T}}$, the linearized forward relationship is

$$\mathbf{d} = G\mathbf{AI} + \mathbf{n}, \tag{5}$$

where $\mathbf{d}$ is the seismic trace vector, $G = WD$ combines a Ricker wavelet convolution matrix W with a finite-difference operator D that maps impedance to reflection coefficients, and $\mathbf{n}$ is noise. Reflection coefficients follow the standard acoustic approximation

$$r_i = \frac{AI_{i+1} - AI_i}{AI_{i+1} + AI_i}. \tag{6}$$

Boundary conditions were imposed as: (i) the top and base of the Middle-Lower Jurassic interval were fixed to well-tied AI values; (ii) at calibration wells, log-derived AI was used as a soft constraint within a ±5% tolerance window; and (iii) outside MF1–MF2 underwater distributary channel and mouth-bar fairways, inverted AI was penalized if it fell below the 10th percentile of the background-shale PDF, suppressing false sand anomalies in mud-prone belts.

3.5.2. Objective Function and Regularization

The trace-wise objective function is

$$J(\mathbf{AI}) = \|\mathbf{d} - G\mathbf{AI}\|_2^2 - \lambda \ln p(\mathbf{AI}), \tag{7}$$

where $p(\mathbf{AI})$ is the AI PDF derived from all calibrated wells and λ is a regularization weight balancing data misfit and log statistics [34]. The optimal impedance is

$$\mathbf{AI}^* = \arg\min_{\mathbf{AI}} J(\mathbf{AI}). \tag{8}$$

The weight λ was selected by leave-one-well-out cross-validation: λ was varied from 0.1 to 2.0 in steps of 0.1, and the value minimizing the root-mean-square error (RMSE) between inverted and log AI at held-out wells was adopted. The optimal value was $\lambda = 0.8$, yielding mean well AI correlation of 0.86 and RMSE of 420 $(\mathrm{g\,cm^{-3}})\,(\mathrm{m\,s^{-1}})$. Thin sand prediction used the combined constraints of (i) inverted AI below the 25th percentile of the channel-sand PDF, (ii) GR $<$ 50 API at wells, and (iii) occurrence within MF1–MF2 microfacies-bounded fairways.

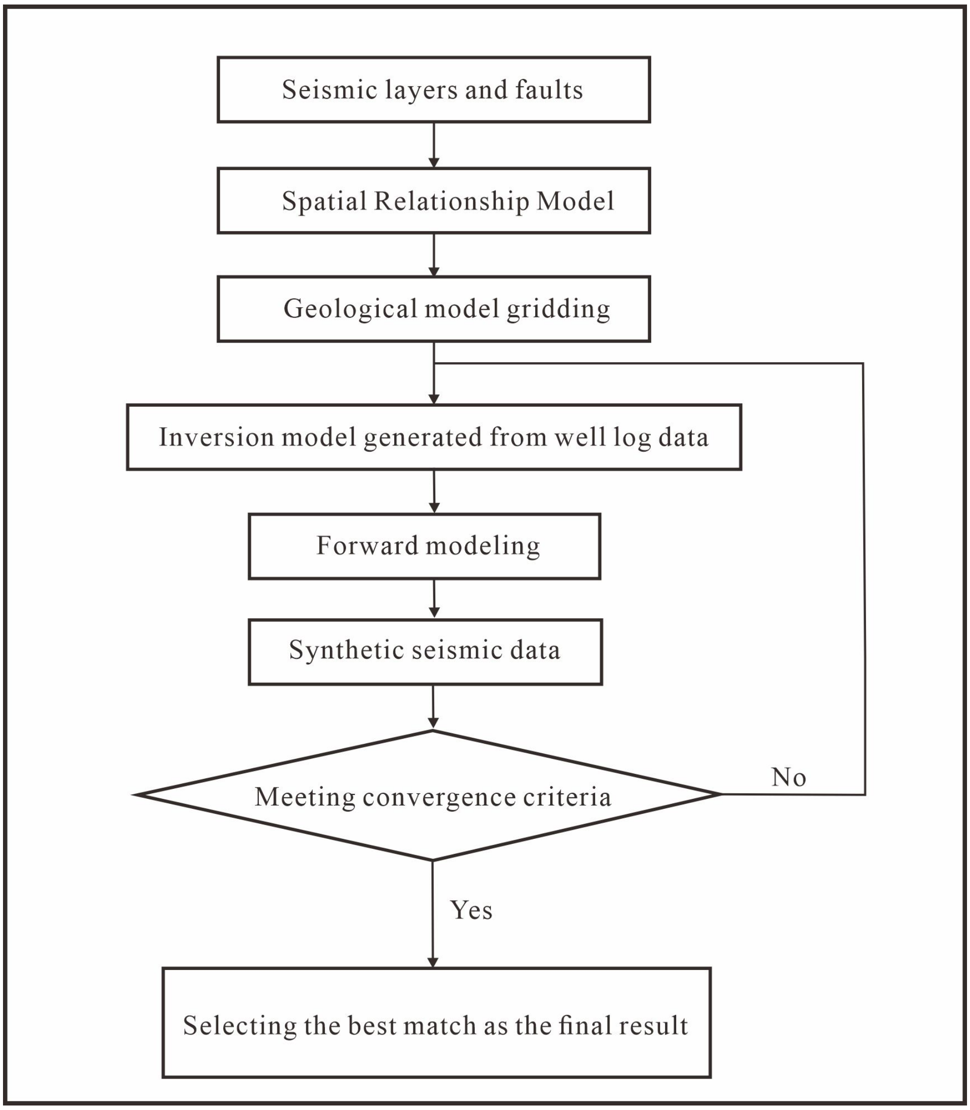

Figure 5. Workflow of stochastic optimization seismic inversion constrained by geological model and well data. Solid arrows show forward/inversion steps; dashed boxes mark geological and well constraints.

3.5.3. Discretization Sensitivity

Because the forward operator G in Equation (1) depends on the temporal sampling of the seismic trace, a discretization sensitivity test was performed. The original 2 ms data and a 4 ms re-sampled volume were inverted independently using identical λ and PDF constraints. At the four calibration wells, mean AI correlation changed from 0.86 (2 ms) to 0.83 (4 ms), and predicted net sand thickness differed by less than 8% in channel centers (Table 3). Lateral sand-body outlines were stable within one seismic trace ($\sim$25 m), indicating that the inversion solution is weakly sensitive to sampling interval within the tested range and that the 2 ms implementation is adequate for thin (<14 m) sand prediction in Block S.

Table 3. Discretization sensitivity of PDF-regularized stochastic optimization inversion. Mean values across calibration wells are shown in bold.

Well	AI Correlation (2 ms)	AI Correlation (4 ms)	Net Sand Thickness Deviation (%)	RMSE (g cm^{-3}) (m s^{-1}), 2 ms/4 ms
S1	0.88	0.84	5.1	395/458
S2	0.87	0.83	7.2	410/472
G1	0.85	0.82	6.8	428/491
N2	0.84	0.81	7.9	447/505
Mean	**0.86**	**0.83**	**6.8**	**420/482**

This approach maintains consistency with both seismic amplitudes and well-log statistics while avoiding explicit variogram modeling (Figure 5).

4. Results

4.1. Sedimentary Facies Characteristics

Core from five wells, combined with grain-size, wireline, and seismic data, reveals a proximal braided river delta–lacustrine assemblage with low compositional maturity. Lithofacies are grouped into three major categories (sandstone, siltstone, and mudstone) and further subdivided using sedimentary-structure codes.

4.1.1. Sandstone Facies

Sandstone is the dominant lithofacies and is mainly medium- to fine-grained, sub-rounded to rounded, and moderately to well sorted, with subordinate coarse and gravelly sandstone (Figure 6). Massive bedding sandstone (Sm) comprises thick, variegated, poorly sorted gravelly coarse-to-medium sandstone with high matrix content and records strong delta-front currents. Trough cross-bedded sandstone (St) and planar cross-bedded sandstone (Sp) form thin gray to grayish-white beds that indicate channel scour and strong unidirectional flow. Parallel-bedded sandstone (Sh), typically 0.2–2 m thick, and associated low-angle cross-bedded sandstone (Sl) occur in stable, high-energy settings and in mouth bars. Scour surfaces (Ss) are thin, fining-upward layers with mud chips and intraclasts that mark erosional channel bases.

4.1.2. Siltstone Facies

Siltstone and argillaceous siltstone are sub-rounded, moderately sorted, and show diverse bedding styles (Figure 7). Lenticular-bedded siltstone (Fcl) contains fine sandstone lenses within argillaceous siltstone and is common in littoral beach bars and shallow-lake sand flats where sand and mud supply alternated. Ripple-bedded and parallel-bedded siltstone (Fc and Fl) record weak or intermittent flow in interdistributary bays and littoral–shallow lake settings. Wavy-bedded siltstone (Fr) and composite-bedded siltstone (also Fc) reflect fluctuating energy in mouth bars, interdistributary bays, and mud flats.

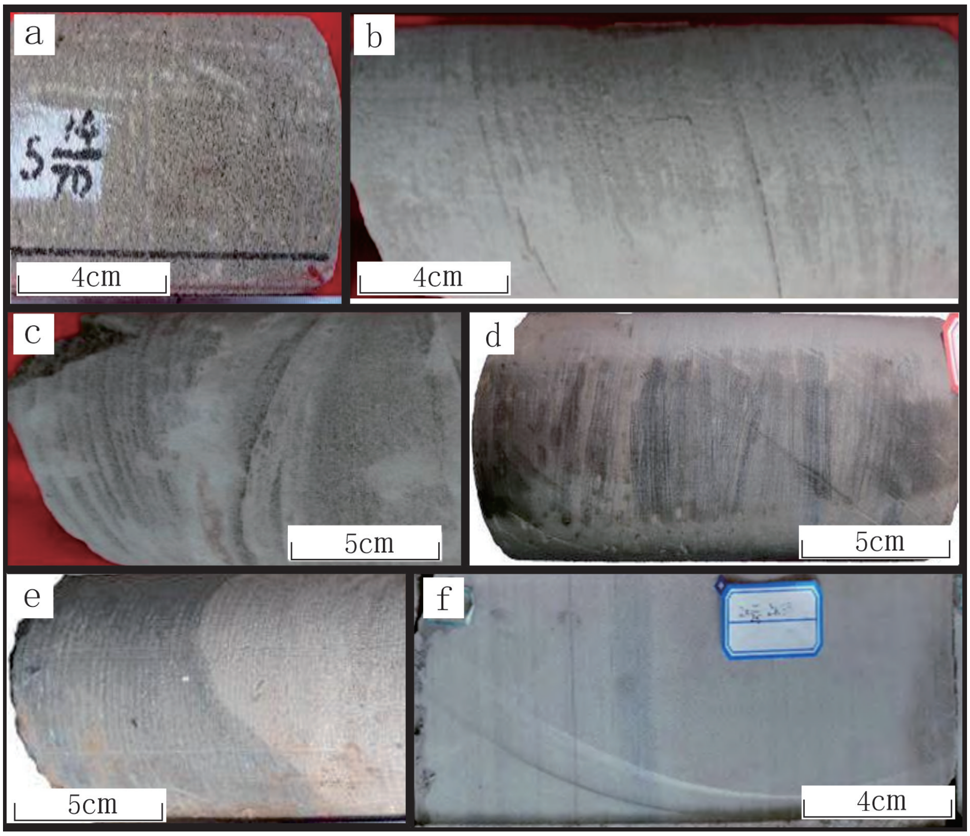

Figure 6. Representative sandstone lithofacies of the Middle-Lower Jurassic in Block S. (**a**) Well S2, 3105.3 m, massive gravelly coarse sandstone; (**b**) Well S1, 3102.7 m, low-angle cross-bedded medium sandstone; (**c**) Well G1, 3201.5 m, trough cross-bedded medium sandstone; (**d**) Well N5, 3180.2 m, planar cross-bedded fine sandstone; (**e**) Well S1, 2995.7 m, scour surface; (**f**) Well S1, 2993.4 m, parallel-bedded fine sandstone.

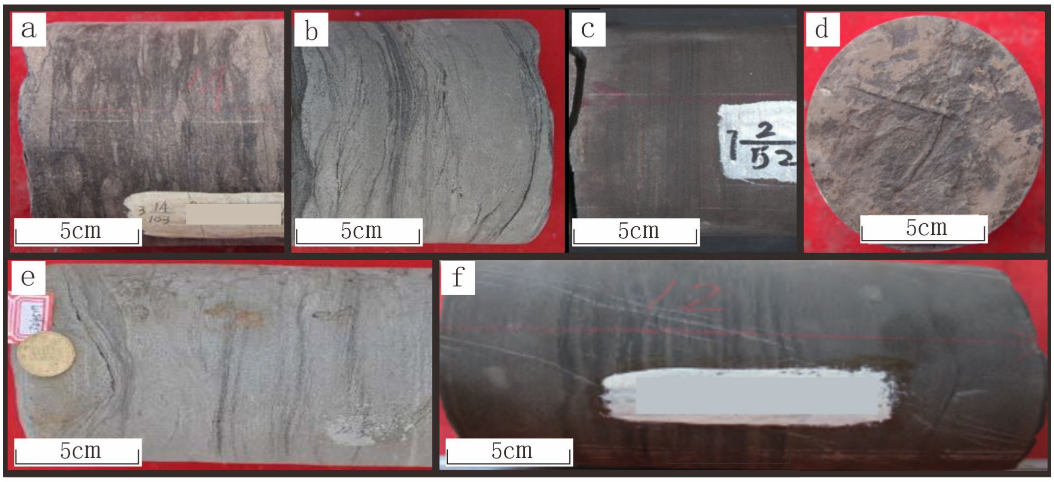

Figure 7. Characteristics of siltstone lithology of the Middle-Lower Jurassic of S area. (**a**) Well S2 (3025.3 m): dark gray siltstone with gray fine sandstone, lenticular bedding; (**b**) Well G1 (3082.7 m): gray siltstone with dark gray argillaceous bands, ripple bedding; (**c**) Well S2 (2879.7 m): dark gray argillaceous siltstone, horizontal bedding; (**d**) Well S2 (2884.7 m): dark gray argillaceous siltstone, plant root debris; (**e**) Well N2 (3045.3 m): grayish-white siltstone, composite bedding; (**f**) Well S2 (2893.4 m): dark gray argillaceous siltstone, wavy bedding.

4.1.3. Mudstone Facies

Mudstone is widely distributed and thick, consisting mainly of black and dark gray mudstone with minor siltstone and fine sandstone interbeds (Figure 8). Massive-bedded mudstone (Mm), locally carbonaceous, accumulated in quiet, reducing settings such as interdistributary bays, littoral muds, and coastal swamps. Horizontally laminated mudstone (Ml) with thin siltstone partings characterizes low-energy interdistributary and littoral–shallow lacustrine environments.

Figure 8. Characteristics of mudstone lithology of the Middle-Lower Jurassic of S area. (**a**) Well S2, depth 2889.3 m: black mudstone with massive bedding; (**b**) Well S2, depth 2990.4 m: black carbonaceous mudstone containing plant leaf fossils; (**c**) Well S1, depth 2969.1 m: grayish-black mudstone intercalated with thin siltstone layers, exhibiting horizontal bedding.

4.1.4. Grain Size Analysis

Grain size reflects the original sedimentary environment and serves as the fundamental basis for analyzing hydrodynamic conditions and classifying sedimentary facies. Sieving analysis of 30 Middle-Lower Jurassic sandstone samples from Block S indicates that most grain sizes range from 0.1 to 1.0 mm (Figure 9). The lithology is dominated by fine and medium sandstones, with minor gravelly coarse sandstones having a maximum gravel diameter reaching 1.5 mm. The grain-size probability cumulative curves fall into three morphological types (Figure 10). One-segment curves are low-slope straight lines with wide grain-size ranges and poor sorting, indicating stable, suspension-dominated transport in subaqueous natural levees or interdistributary bays. Two-segment curves combine saltation and suspension populations and split into low-slope and high-slope forms. Low-slope two-segment curves record moderate sorting and wide grain-size ranges in high-energy delta-plain channels and underwater distributary channels, whereas high-slope two-segment curves have steep saltation segments, good sorting, and fine sandstone–siltstone assemblages typical of mouth bars under relatively weak but persistent flow.

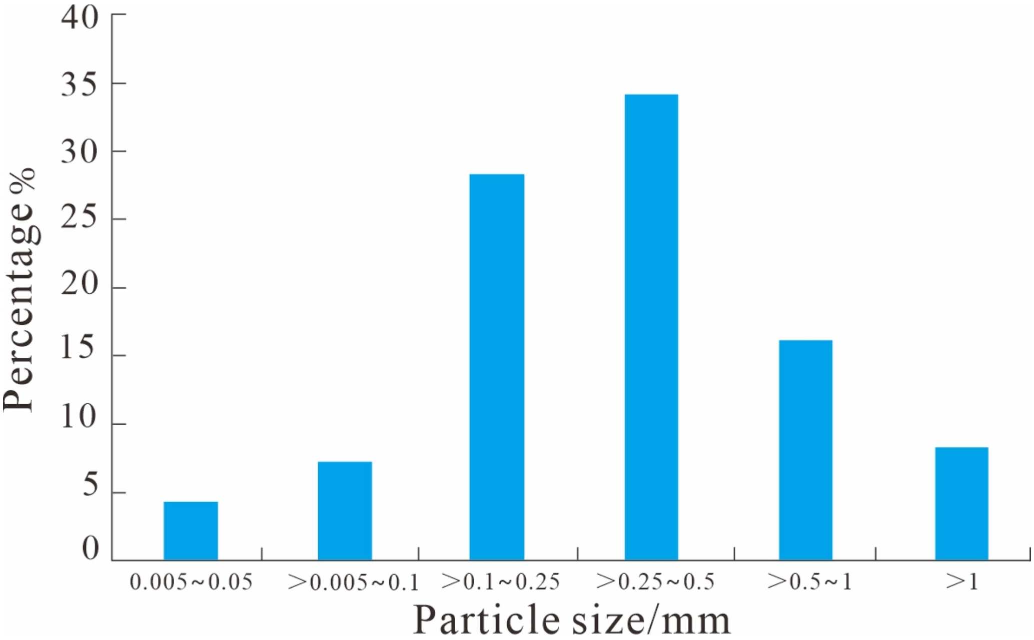

Figure 9. Histograms of grain size distribution in the Middle-Lower Jurassic of S area on the right bank of the Amu Darya.

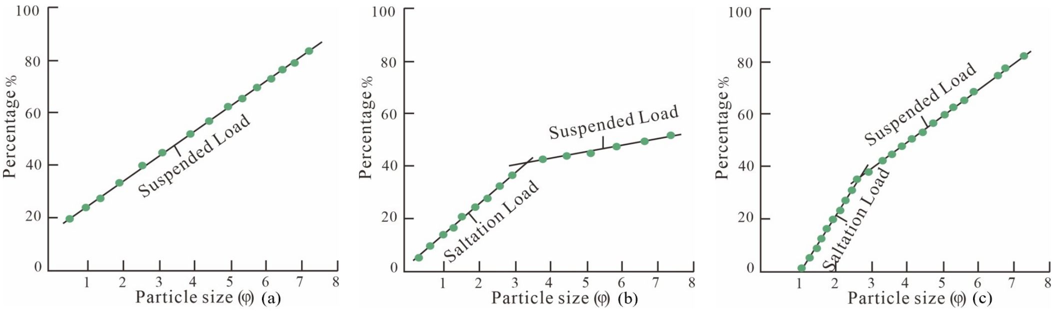

Figure 10. Grain size cumulative probability curves of delta subfacies in Block S. (**a**) One-segment pattern; (**b**) low-slope two-segment pattern; (**c**) high-slope two-segment pattern.

4.1.5. Log Facies Characteristics

Correlation of cores and logs from four wells defines five electrofacies (Figure 11). Box-shaped logs show flat, low SP, low GR, and high resistivity over uniform gravelly coarse to medium sandstone with abrupt mudstone contacts, recording stable, high-energy underwater distributary channels. Bell-shaped logs fining upward from coarse to fine sandstone and siltstone mark waning channel flow and abandonment into interdistributary bays. Funnel-shaped logs coarsen upward from mudstone to fine sandstone and siltstone and typify mouth-bar progradation. Finger-shaped logs intercalate thin sandstone beds within thick mudstone and correspond to beach bars or coal-bearing littoral swamps. Straight, near-baseline SP with high GR and low resistivity over thick mudstone indicates quiet littoral or shallow-lake mud flats.

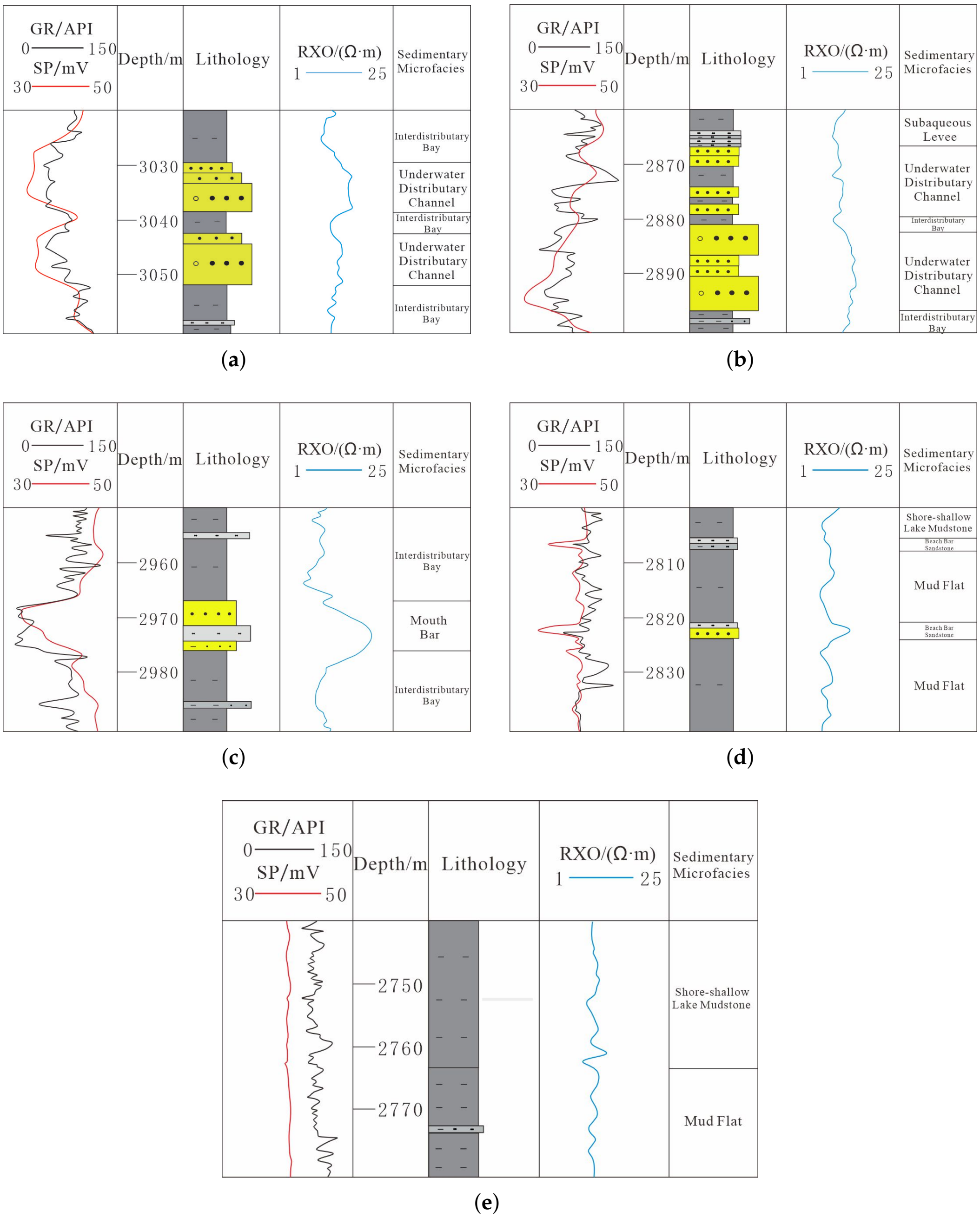

Figure 11. Log facies characteristics of the Middle-Lower Jurassic in Block S. Tracks show GR (green), SP (blue), and deep resistivity (red); lithology columns use standard patterns. (**a**) Box-shaped; (**b**) bell-shaped; (**c**) funnel-shaped; (**d**) finger-shaped; (**e**) straight.

4.1.6. Seismic Facies Characteristics

Seismic profiles were classified into parallel to sub-parallel, lenticular, and chaotic/progradational facies according to reflection geometry and amplitude (Figure 12). Parallel to sub-parallel, medium- to high-continuity reflections correlate with mud-prone lithologies and finger-shaped or linear logs in interdistributary bays and shallow-lake mud flats. Lenticular, irregular reflections with coarsening-upward logs mark mouth bars. Chaotic, sigmoid-clipping wedge bodies with downlap and box-to-bell log motifs represent stacked underwater distributary channels.

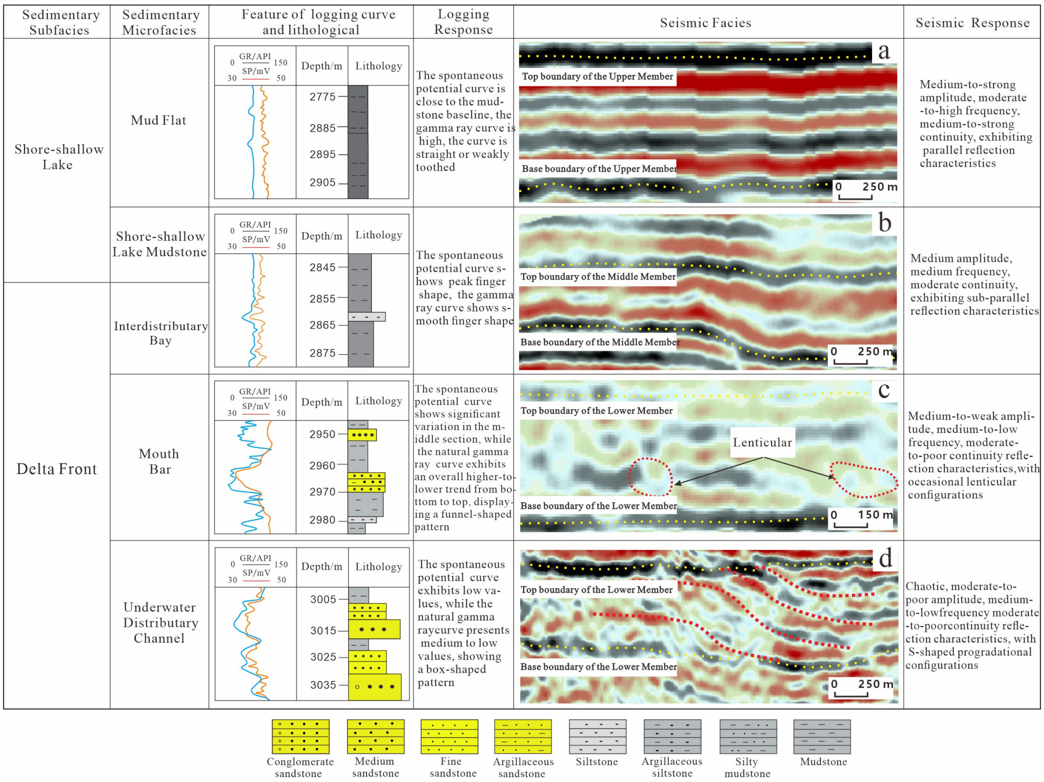

Sedimentary Subfacies	Sedimentary Microfacies	Feature of logging curve and lithological	Logging Response	Seismic Facies	Seismic Response
Shore-shallow Lake	Mud Flat		The spontaneous potential curve is close to the mudstone baseline, the gamma ray curve is high, the curve is straight or weakly toothed		Medium-to-strong amplitude, moderate-to-high frequency, medium-to-strong continuity, exhibiting parallel reflection characteristics
	Shore-shallow Lake Mudstone		The spontaneous potential curve shows peak finger shape, the gamma ray curve shows smooth finger shape		Medium amplitude, medium frequency, moderate continuity, exhibiting sub-parallel reflection characteristics
Delta Front	Interdistributary Bay				
	Mouth Bar		The spontaneous potential curve shows significant variation in the middle section, while the natural gamma ray curve exhibits an overall higher-to-lower trend from bottom to top, displaying a funnel-shaped pattern		Medium-to-weak amplitude, medium-to-low frequency, moderate-to-poor continuity reflection characteristics,with occasional lenticular configurations
	Underwater Distributary Channel		The spontaneous potential curve exhibits low values, while the natural gamma raycurve presents medium to low values, showing a box-shaped pattern		Chaotic, moderate-to-poor amplitude, medium-to-lowfrequency moderate-to-poorcontinuity reflection characteristics, with S-shaped progradational configurations

Figure 12. Seismic facies characteristics of the Middle-Lower Jurassic in Block S. (**a**) Parallel reflections (littoral–shallow-lake mudstone); (**b**) sub-parallel reflections (interdistributary bay); (**c**) lenticular reflections (mouth bar); (**d**) chaotic progradational wedges (underwater distributary channel). Well logs (GR/SP) are overlain in color.

4.2. Types of Sedimentary Microfacies

Integration of lithofacies, logs, and seismic data shows that the Middle-Lower Jurassic in Block S comprises delta front, littoral lake, and shallow lake subfacies subdivided into nine numbered microfacies (MF1–MF9; Table 2). The delta front includes MF1 (underwater distributary channel), MF2 (mouth bar), MF3 (interdistributary bay), and MF4 (subaqueous natural levee). The littoral lake includes MF5 (beach bar), MF6 (littoral mud), and MF7 (coastal swamp). The shallow lake includes MF8 (sand flat) and MF9 (mud flat).

MF1 (underwater distributary channel) comprises subaqueous extensions of onshore channels, less than 20 m thick, built of multi-stage, well-rounded gravelly to medium–fine sandstone fining upward from massive, cross-, and parallel-bedded bases with scour surfaces into siltstone and mudstone, with box- or bell-shaped logs and medium-low GR. MF2 (mouth bar) at channel mouths consists of well-sorted fine sandstone and siltstone coarsening upward from horizontal to ripple bedding, with serrated funnel-shaped SP, GR, and resistivity curves. MF3 (interdistributary bay) between channels is mudstone-dominated with subordinate laminated fine sandstone and straight, high-GR log motifs. MF4 (subaqueous natural levee) forms thin fine sandstone and siltstone sheets flanking channel margins under waning flow, with finger-shaped GR and one-segment grain-size curves. MF5 (beach bar) comprises thin littoral siltstone bodies with lenticular bedding and finger-shaped GR and SP responses. MF6 (littoral mud) and MF7 (coastal swamp) are low-energy littoral settings yielding thick dark to carbonaceous mudstone; MF7 additionally contains thin coal seams, roots, and bioturbation. MF8 (sand flat) and MF9 (mud flat) occur in distal shallow-lake settings; MF8 consists of thin siltstone within dark mudstone with finger-shaped logs, whereas MF9 is mudstone-dominated with straight, high-GR responses.

4.3. Single-Well and Cross-Well Sedimentary Facies Analysis

Single-well facies analysis of the Middle-Lower Jurassic in Well S2 (Figure 13) shows a fining-upward succession of fine sandstone, siltstone, and mudstone in which sand-body frequency and thickness decrease upward, recording transgression and rising lake level. The Lower Member is dominated by underwater distributary channels with thick medium to fine sandstone and serrated box- and bell-shaped GR curves. The Middle Member passes into littoral-lake beach bars, littoral muds, and coastal swamps with siltstone, mudstone, coal, and funnel- to bell-shaped GR motifs under weaker hydrodynamics. The Upper Member is mainly shallow-lake mud and sand flats with finger-shaped or linear GR curves, but late regression reintroduced delta-front mouth bars and small underwater distributary channels with funnel- and bell-shaped GR responses.

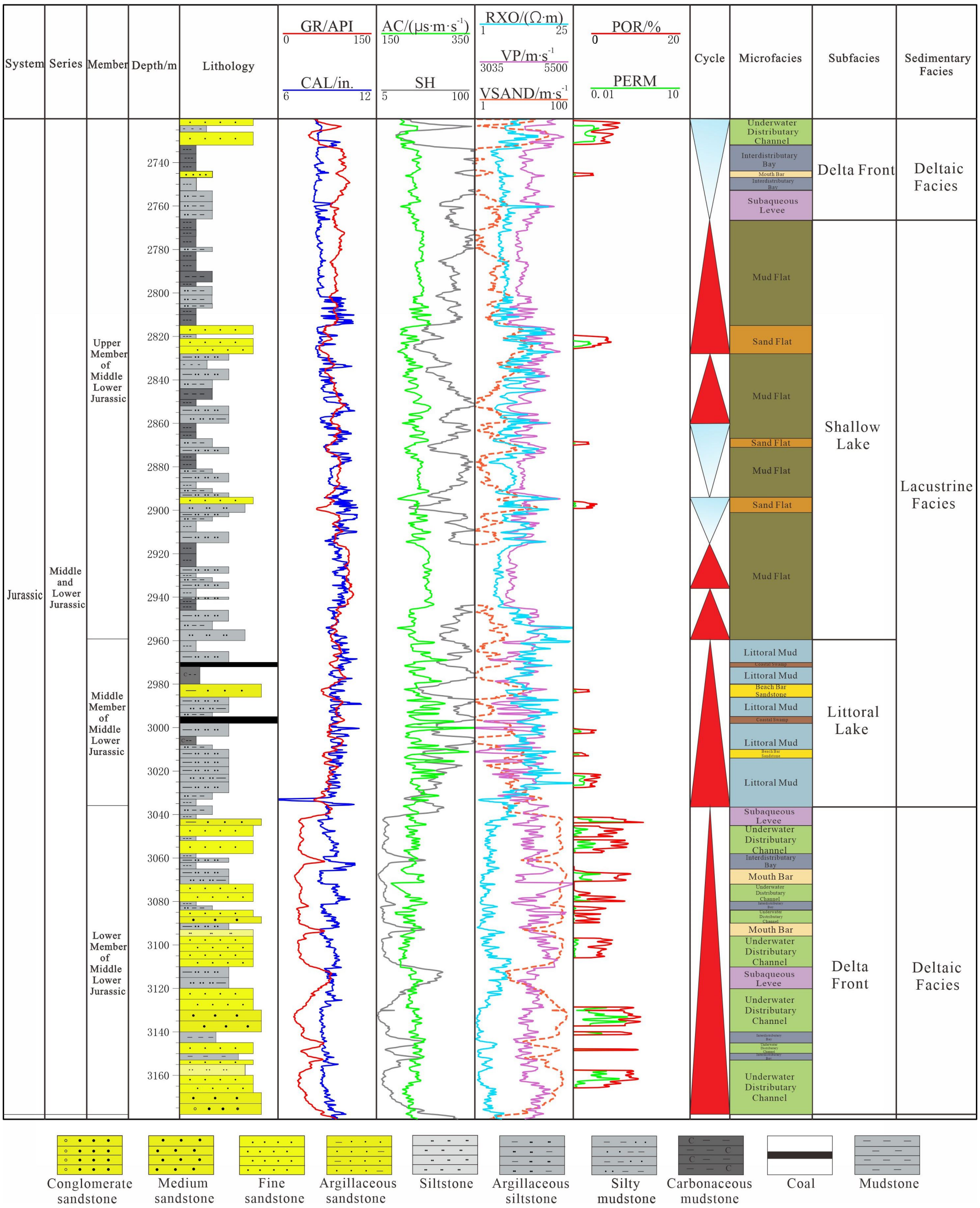

Figure 13. Single-well sedimentary facies characteristics of the Middle-Lower Jurassic in Well S2, Block S.

Delta front deposits exhibit a northeastward retrogradational trend in the cross-well correlation (Figure 14). During Lower Member deposition, low lake levels and abundant northeastern sediment supply formed extensive proximal underwater distributary channels with thick medium-to-fine sandstones in the northern S-x and eastern G-x and N-x blocks, together with distal mouth bars in the western P-x block. Middle Member transgression shifted the area into a littoral lake environment dominated by siltstones and mudstones with minor coal seams. Early Upper Member transgression expanded the basin to maximum extent with thick shallow-lake mudstones. Late Upper Member regression re-established the delta front across the study area.

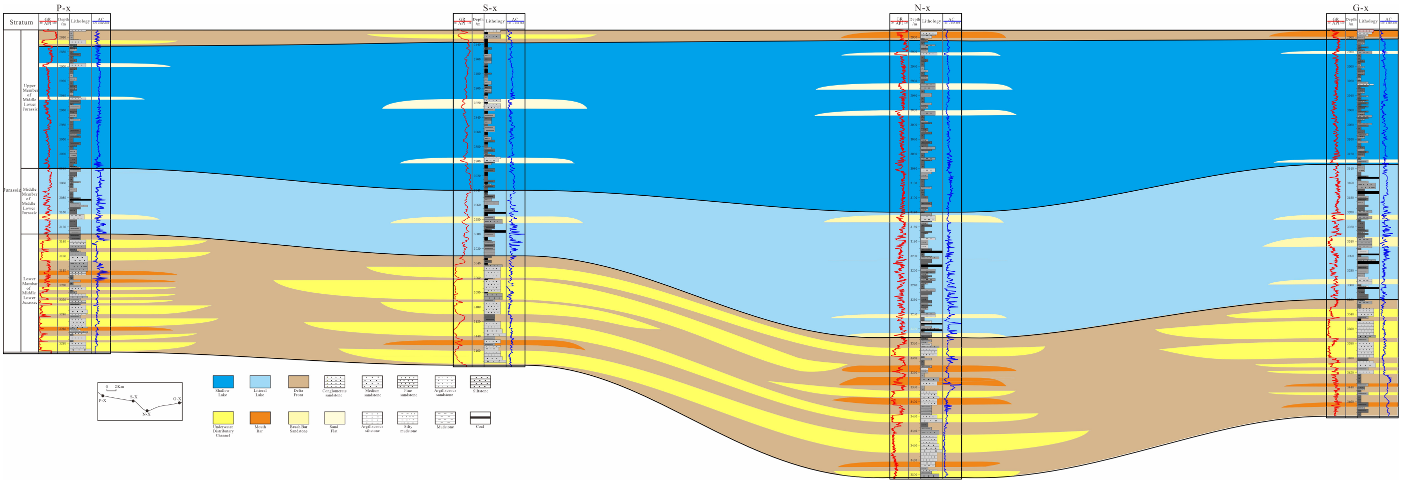

Figure 14. Cross-well sedimentary facies correlation of the Middle-Lower Jurassic in Block S. Gray shading denotes mud-prone intervals; colored bars mark sand-prone facies belts.

4.4. Planar Distribution Characteristics of Sedimentary Microfacies

The Middle-Lower Jurassic succession in Block S records a braided river delta system that evolved from progradation to retrogradation and back to progradation, primarily in response to lake-level change and variable sediment supply.

During Lower Member deposition, the lake basin was expanding under relatively stable tectonics and strong northern provenance supply. Paleoslope was steeper in the north, favoring littoral–shallow lacustrine settings. Large underwater distributary channels extended southward in belt-like and anastomosing patterns, with mouth bars forming at channel bifurcations. This interval contains the widest sand-body distribution, best lateral connectivity, and highest sand–mud ratio in the study area (Figure 15a).

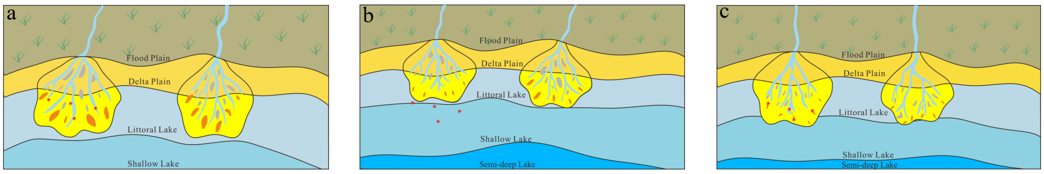

Figure 15. Planar distribution of sedimentary microfacies in Block S. Stars mark well locations; colors distinguish microfacies types (see Table 2). (**a**) Lower Member; (**b**) Middle Member; (**c**) late Upper Member.

Middle Member deposition was dominated by lacustrine transgression. Rising base level expanded the semi-deep lake southward and forced delta-front retrogradation toward the provenance. Underwater distributary channels became shorter, laterally restricted, and less continuous, while wave reworking reduced the preservation of distal mouth bars and increased mudstone proportion (Figure 15b).

Late Upper Member regression reactivated delta-front progradation. Delta lobes expanded southward again, and underwater distributary channels increased in scale and bifurcation frequency, re-establishing a laterally extensive sand-body network with renewed mouth-bar development (Figure 15c). Collectively, these stages explain the strong vertical and lateral heterogeneity of Middle-Lower Jurassic reservoirs in Block S.

4.5. Sedimentary Model

The evolution of braided river deltas is controlled by tectonics, paleogeomorphology, lake level, and sediment supply. Analysis of the Middle-Lower Jurassic reveals braided river delta front, littoral lake, and shallow lake subfacies. An overall upward-fining sequence reflects a transgressive process, establishing a retrogradational braided river delta front sedimentary model.

During the Lower Member deposition, strengthened rift activities created steep slope zones within a relatively small lake basin. High northern elevation differences and a humid climate provided abundant sediment. Strong hydrodynamics drove extensive underwater distributary channels, forming belt-like patterns proximally and finger-like strips distally. Strong progradation, frequent avulsion, and deep vertical incision formed multi-period superimposed channels with mouth bars at bifurcation points (Figure 16a).

During the Middle Member deposition, a rapid lake level rise deepened the water and weakened sediment supply. The delta front retrograded landward, significantly reducing channel extension, scale, and thickness. Vertically, the sequence manifests as thick mudstones intercalated with thin siltstones, dominated by littoral-shallow lake muds with sporadic beach bar sands (Figure 16b).

By the late Upper Member deposition, a regression gradually lowered lake levels and decreased accommodation space. Continuous sediment supply and strong hydrodynamics forced the delta front to prograde basinward again. Underwater distributary channels rebounded in scale and extension, with frequent bifurcations and lateral swinging forming open, lobe-like distributions that covered earlier semi-deep lake areas. Vertically, thicker progradational sand bodies, along with developed mouth and beach bars, improved lateral connectivity to form another favorable reservoir interval succeeding the Lower Member (Figure 16c).

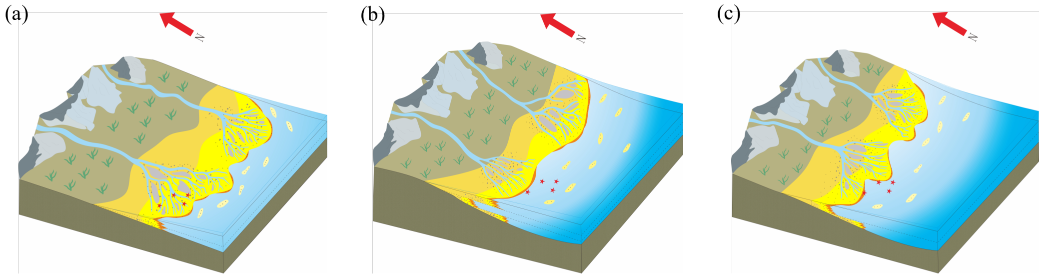

Figure 16. Retrogradational–progradational sedimentary model of the Middle-Lower Jurassic in Block S. Stars indicate well control; colors denote subfacies belts. (**a**) Lower Member; (**b**) Middle Member; (**c**) late Upper Member.

4.6. Prediction of Reservoir Distribution

Reservoir quality in Block S is strongly facies-controlled, with MF1 underwater distributary channels and MF2 mouth bars forming the primary fairways [3,24]. Guided by planar microfacies boundaries (Figure 15), stochastic optimization inversion was performed on steerable-pyramid-enhanced seismic data. Using GR $<$ 50 API as the reservoir cutoff, low-impedance anomalies agree with sand intervals at wells (Figure 17a), confirming that geological constraints and PDF-regularized inversion jointly improve thin-sand detectability relative to unconstrained approaches [3,10]. The cross-well profile reveals rapid lateral facies change at channel margins and interchannel areas.

The predicted thickness map (Figure 17b) shows favorable sands in strip-like, lobate, and interconnected patterns, with maximum thickness of 14 m along underwater distributary channel axes and mouth-bar intersections—morphologies comparable to channel fairways mapped in fan-delta SWII studies [3,11]. These results provide a quantitative basis for lithologic trap screening and well placement in Block S.

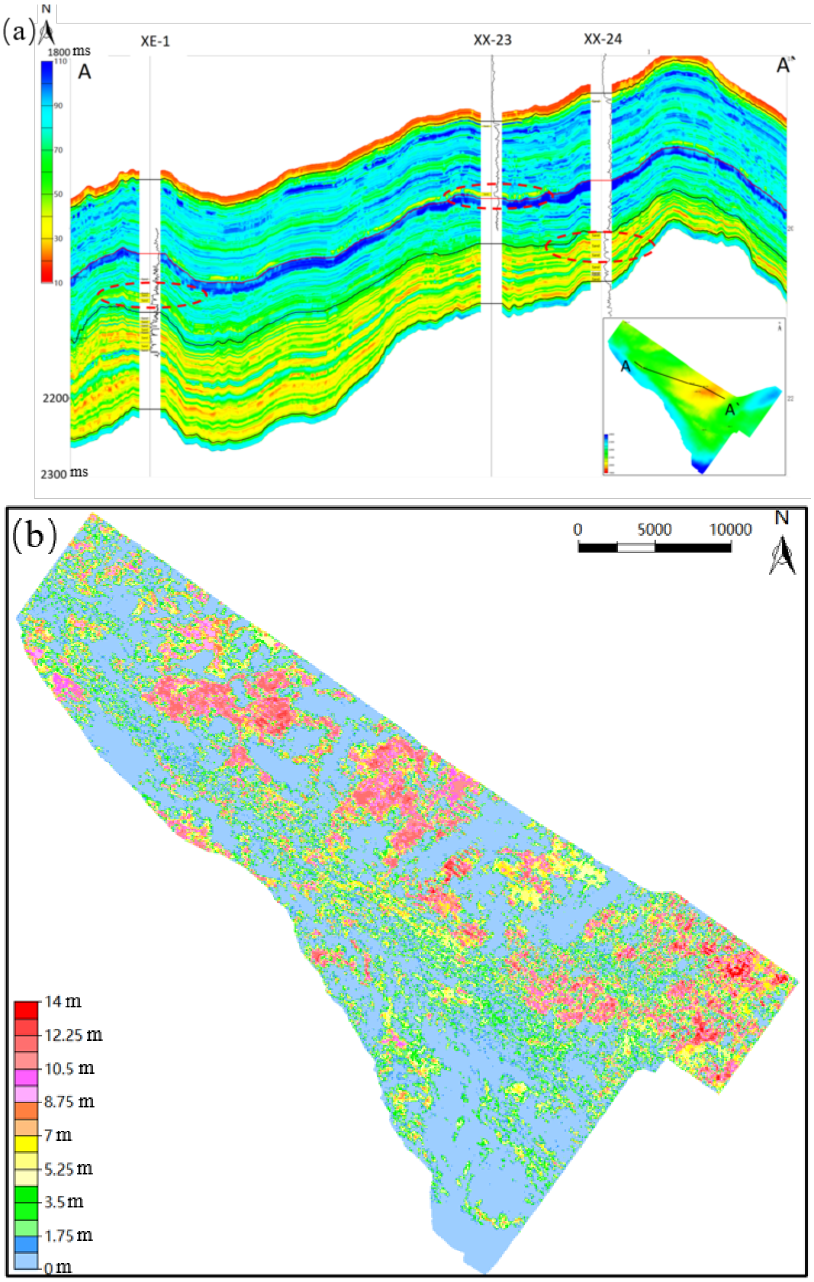

Figure 17. Reservoir prediction results based on stochastic optimization inversion. (**a**) Cross-well stochastic inversion profile (A–A′) across wells XE-1, XX-23, and XX-24; warm colors indicate low acoustic impedance (sand-prone) and cool colors high impedance (mud-prone); circles mark well locations. (**b**) Planar distribution map of predicted reservoir thickness (m); warm colors denote thicker sands; north arrow and distance scale in upper right.

4.7. Comprehensive Evaluation of Favorable Facies Belts

Based on the core observation of five wells in the study area, combined with physical property data and casting thin section analysis, the favorable reservoir facies belts in the study area are divided into three categories (Table 1).

Type I reservoirs (MF1) formed under strong hydrodynamic conditions and are dominated by gravelly to medium sandstone with low matrix content, well-developed intergranular and dissolution pores, and superior pore-throat connectivity. Type II reservoirs (MF2) consist of well-sorted fine sandstone with moderate mud content and calcite cement, yielding residual intergranular and dissolution porosity. Type III reservoirs (MF5) are silt-dominated, mud-rich, and poorly porous.

Middle-Lower Jurassic littoral–shallow lake mudstones, carbonaceous mudstones, and coal seams constitute effective source rocks (TOC $> 1\%$; Type III kerogen; R_o = 0.8–2.5%), generally in the over-mature stage with peak generation during the Paleogene. Together with Type I and Type II reservoirs, they form a favorable source–reservoir–cap assemblage in Block S.

5. Discussion

5.1. Comparison with Regional Sedimentary Models

Regional studies describe the Middle-Lower Jurassic as a proximal, delta-front to littoral–shallow lacustrine system [15,18,23,24]. Block S refines this framework by showing that reservoirs concentrate in underwater distributary channels and mouth bars, with beach bars subeconomic—a pattern analogous to subaqueous channel fairways in geologically constrained fan-delta inversion [3]. Two sand-rich progradational intervals separated by a transgressive mudstone unit support a retrogradational–progradational model controlled by lake-level change and channel avulsion [24,28].

Compared with the Mahu Sag workflow [3], Block S differs in depositional system (braided river delta–lacustrine versus fan delta) and inversion engine (steerable pyramid plus PDF-regularized stochastic optimization versus SWII), yet both studies emphasize that planar microfacies boundaries must constrain inversion to reduce uncertainty in thin, heterogeneous sands. The present case extends this philosophy to a deeper, near-basement gas play in Central Asia.

5.2. Exploration Implications

The identification of Type I and Type II facies belts has direct exploration significance. Lower Member and late Upper Member intervals should be prioritized for lithologic trap screening because they combine wide channel-sand distribution with the best petrophysical properties. In contrast, Middle Member littoral–shallow lacustrine mudstones, although poor reservoirs, act as regional seals and high-quality source rocks, reinforcing the source–reservoir–cap logic previously proposed for the Right Bank [18,23].

The thickness map and cross-well inversion profile indicate that favorable sands are not uniformly distributed along structure but follow channel-axis and channel-intersection geometries. This pattern suggests that future drilling should target seismic-enhanced linear anomalies with low GR and low AI responses rather than broad structural highs alone. Such a facies-guided approach is particularly relevant in Block S, where fault compartmentalization and facies change can decouple reservoir presence from structural elevation [27].

5.3. Methodological Significance

The main geophysical contribution is sequential coupling of microfacies constraints, steerable pyramid enhancement, and PDF-regularized stochastic inversion—complementary to navigation-pyramid and waveform-inversion workflows applied in other continental basins [4,5,36]. Pre-inversion enhancement improved channel continuity (Figure 4); PDF constraints avoided explicit variogram modeling in a five-well calibration setting [7,35,37,38]. The workflow is transferable to other deep, heterogeneous clastic gas fields where facies-guided inversion is required [25,39,40].

5.4. Limitations and Future Work

Several limitations should be noted. The Middle-Lower Jurassic in Block S remains data-limited: only five cored wells and four fully calibrated log suites constrain a large 3D seismic volume, so additional penetration would strengthen facies boundaries and inversion calibration. The target interval also lies close to the acoustic basement, where bandwidth and signal-to-noise ratio are low and lateral extent of thin sands remains uncertain. Discretization tests (2 ms versus 4 ms sampling; Table 3) indicate stable sand-body outlines, but finer grid sensitivity was not explored beyond these intervals. Moreover, although GR-based reservoir cutoff and AI inversion agree at wells, absolute porosity prediction was not attempted and would require further rock-physics modeling.

Future work should integrate newly drilled well data as they become available, apply advanced pre-stack reprocessing to improve near-basement imaging, and incorporate outcrop or analog-basin datasets to reduce model uncertainty. Coupling the present facies model with dynamic flow simulation would further test the exploration significance of identified channel networks. As additional wells and seismic coverage accrue in Block S, complementary data-analytic tools from adjacent disciplines may help extend—rather than replace—the facies-guided inversion framework established here. Metaheuristic optimizers that have stabilized parameter searches in other inverse problems [41–45] could be tested for refining λ and PDF weights under the same five-well calibration constraint. For quality control of thin sand picks on slice displays and at well ties, object-detection, CNN–Transformer, stacked-ensemble, and unsupervised anomaly-screening schemes [46–51] merit pilot application to channel-margin segments where facies change most rapidly. Multi-view tensor fusion and PDE-based segmentation workflows [52–57] may further assist ranking of post-stack attributes within mapped MF1–MF2 belts, and edge-aware electrofacies classifiers [58–60] could accelerate log auditing in future penetration. Sparse-control geometric reconstruction [61] may also support template gridding of fault-bounded fairways before the next inversion cycle.

6. Conclusions

This study presents an integrated sedimentological and geophysical characterization of the Middle-Lower Jurassic braided river delta–lacustrine system in Block S of the Amu Darya Right Bank. Integrated core, grain-size, log, and seismic data define three subfacies and nine numbered microfacies (MF1–MF9; Table 2), among which MF1–MF2 delta-front associations host the main reservoirs. Vertically, Lower Member progradational channel sands gave way to middle–early Upper Member transgressive lacustrine fines and then to late Upper Member delta-front re-establishment, yielding two sand-prone intervals separated by regional seal-prone mudstones. Fault-controlled graben–horst paleotopography (Figure 2) influenced provenance delivery and sand fairway distribution. Petrophysical ranking places MF1 underwater distributary channels (Type I; average porosity 12.7%) and MF2 mouth bars (Type II; 10.1%) as the most favorable facies belts, with sand-ratio cutoffs validated against core. Coupled steerable pyramid enhancement

($K = 4$ scales, $N = 6$ orientations) and PDF-regularized stochastic optimization inversion ($\lambda = 0.8$) improve channel-sand imaging and map reservoir thickness (m) along channel axes and intersections, providing a transferable workflow for deep clastic gas exploration in Central Asia.

Author Contributions: Conceptualization, F.L. and Y.X.; methodology, F.L. and Y.X.; software, F.L.; validation, F.L., Y.X. and X.H.; formal analysis, F.L.; investigation, F.L., H.L., Y.L., Z.W., N.Z., R.L. and B.L.; resources, Y.X. and X.H.; data curation, F.L.; writing—original draft preparation, F.L.; writing—review and editing, Y.X. and X.H.; visualization, F.L.; supervision, Y.X.; project administration, Y.X.; funding acquisition, Y.X. All authors have read and agreed to the published version of the manuscript.

Funding: This work was supported by the General Program of the National Natural Science Foundation of China (Grant No. 42574188), the National Key R&D Program of China (Grant No. 2025YFE0212900), and the National Major Special Project of China (Grant No. 2025ZD1400400).

Institutional Review Board Statement: Not applicable.

Informed Consent Statement: Not applicable.

Data Availability Statement: The data that support the findings of this study are available from the corresponding author, Yungui Xu, upon reasonable request.

Acknowledgments: The authors thank PetroChina International (Turkmenistan) Amu Darya Gas Company for permission to publish this work and the reviewers for constructive comments. The author(s) used ChatGPT-4o (OpenAI, May 2024) only for English language polishing; all scientific content was written and verified by the authors, who take full responsibility for this publication.

Conflicts of Interest: Author Haotong Liu was employed by PetroChina Safety and Environmental Protection Technology Research Institute. Authors Youheng Leng, Zhanjun Wei, and Ronghe Liu were employed by PetroChina International (Turkmenistan) Amu Darya Gas Company. Authors Nini Zhang and Boyong Liao were employed by Geological Exploration and Development Research Institute of CNPC Chuanqing Drilling Engineering Company. The remaining authors declare that the research was conducted in the absence of any commercial or financial relationships that could be construed as a potential conflict of interest. The funders had no role in the design of the study; in the collection, analyses, or interpretation of data; in the writing of the manuscript; or in the decision to publish the results.

References

1. Zeng, H. High-resolution mapping of subsurface sedimentary facies and reservoirs using seismic sedimentology. *Appl. Sci.* **2025**, *15*, 6387. [CrossRef]
2. He, Z.; Li, J.; Wang, H.; Chen, Y.; Zhang, L. Seismic sedimentology for the characterization of Quaternary evaporite facies in biogas-bearing Taidong area, Sanhu Depression, Qaidam Basin, NW China. *Appl. Sci.* **2025**, *15*, 2288. [CrossRef]
3. Wang, J.; Chen, X.; Liu, X.; Huang, Y.; Su, A. Prediction of favorable sand bodies in fan delta deposits of the second member in Baikouquan Formation, X Area of Mahu Sag, Junggar Basin. *Appl. Sci.* **2025**, *15*, 10908. [CrossRef]
4. Wang, J.; Guan, D.; Huang, X.; He, Y.; Li, H.; Xu, W.; Liu, R.; Feng, B. Integrated SOM multi-attribute optimization and seismic waveform inversion for thin sand body characterization: A case study of the Paleogene Lower E3d2 sub-member in the HHK Depression, Bohai Bay Basin. *Appl. Sci.* **2025**, *15*, 5134.
5. Liu, S.; Zhou, L.; Zhang, B.; Dai, R.; Lu, P.; He, C.; Wu, Y.; Ni, C. Thin-layer siliceous dolomite prediction based on post-stack seismic data mining and optimization. *Appl. Sci.* **2025**, *15*, 9631.
6. Li, H. Microfacies analysis of braided river deposits based on seismic-to-well ties: A case study of the Jin-77 well block in the Dongsheng gas field, Ordos Basin. *Oil Gas Geol.* **2025**, *46*, 91–107. (In Chinese)
7. Grana, D.; Della Rossa, E.; Colombo, D. Stochastic inversion of seismic data for reservoir properties: A review. *Geophysics* **2012**, *77*, R23–R34. [CrossRef]
8. Grana, D.; Mukerji, T. *Introduction to Geophysical Integration and Machine Learning: Seismic Reservoir Characterization*; Cambridge University Press: Cambridge, UK, 2021.

9. Xue, Y.; Sen, M.K. Stochastic seismic inversion using greedy annealed importance sampling. *J. Geophys. Eng.* **2016**, *13*, 786–804. [CrossRef]
10. Xu, Y.; Bai, C.; Zhang, R.; Chen, G.; Wu, L.; Huang, X. Prediction of thin sand body reservoirs using facies-model-constrained stochastic optimization inversion. *Front. Earth Sci.* **2026**, *14*, 1754981.
11. Norum, A.; Abedi, M.; Kharrat, R. Seismic prediction of porosity in the Norne field: Utilizing support vector regression and empirical models driven by Bayesian linearized inversion. *Appl. Sci.* **2025**, *15*, 616. [CrossRef]
12. Alves Gomes, N.S.; Grana, D.; Azevedo, L. Advanced elastic and reservoir properties prediction through generative adversarial network. *Appl. Sci.* **2023**, *13*, 6311. [CrossRef]
13. Gharibian, A.; Mukerji, T.; Grana, D. Lithology and porosity distribution of high-porosity sandstone reservoir in North Adriatic using machine learning synthetic well catalogue. *Appl. Sci.* **2023**, *13*, 7671. [CrossRef]
14. Tasikyn, A.; Li, J.H.; Li, H.L.; Li, W.B.; Mao, X.; Wang, H.H. Tectonic evolution and petroliferous characteristics of basin groups in Central Asia and adjacent regions. *Geoscience* **2014**, *28*, 573–584. (In Chinese)
15. Zhang, T.; Li, J.; Wang, H. A study on the sedimentary environment and facies model of Triassic carbonate rocks in the Mangeshlak Basin. *Appl. Sci.* **2025**, *15*, 7788. [CrossRef]
16. Guo, Y.Q.; Liu, L.F.; Zhu, S.L. Classification and assessment of petroleum system in Amu-Darya Basin. *Pet. Explor. Dev.* **2006**, *33*, 515–520. (In Chinese)
17. He, Y.D.; Wei, C.G. Tectonic evolution and its vital role for oil and gas reservoir in Amu Darya Basin. *Prog. Geophys.* **2014**, *29*, 1143–1147. (In Chinese)
18. Li, H.W.; Tong, X.G.; Wang, S.H.; Gao, X.K.; Wen, Z.X.; Guo, J.Y. An analysis of geological characteristics and exploration potential of the Jurassic play, Amu Darya Basin. *Nat. Gas Ind.* **2010**, *30*, 6–12. (In Chinese)
19. Zhang, B.; Zheng, R.C.; Liu, H.N.; Wu, L.; Chen, R.J. Characteristics of carbonate reservoir in Callovian-Oxfordian of Samandepe Gas Field, Turkmenistan. *Acta Geol. Sin.* **2010**, *84*, 117–125. (In Chinese)
20. Xu, W.L.; Zheng, R.C.; Fei, H.Y.; Sun, Z.J.; Wang, Q. The sedimentary facies of Callovian-Oxfordian in Amu Darya basin, Turkmenistan. *Geol. China* **2012**, *39*, 954–964. (In Chinese)
21. Lv, G.X.; Liu, H.N.; Deng, M.M.; Wu, L.; Cheng, X.B.; Zhang, X.Y.; Liu, Y.C. *Exploration and Development of Giant Carbonate Gas Field in the Amu Darya Right Bank Area*; Science Press: Beijing, China, 2013. (In Chinese)
22. Tian, Y.; Xu, H.; Zhang, X. Sedimentary characteristics, distribution regularities and main controlling factors of carbonate intra-platform shoal reservoirs: A case study of intra-platform shoal gas fields in the Amu Darya Basin. *Earth Sci. Front.* **2017**, *24*, 312–321.
23. Chang, H.L.; Rong, C.Z.; Wang, Q. Characteristics of lower-middle Jurassic sandstone reservoirs in Amu Darya Basin, Turkmenistan. *Oil Gas Geol.* **2015**, *36*, 985–993. (In Chinese)
24. Zhang, T.; Wang, Q.; Liu, B. Sedimentary facies and its lateral distribution of the Middle-Lower Jurassic in Amu Darya right bank area. *J. Xi'an Shiyou Univ.* **2014**, *36*, 27–38. (In Chinese)
25. Qi, Y.; Hu, Z.; Wang, J.; Zhang, F.; Wang, X.; Hu, H.; Wang, Q.; Wang, H. The formation mechanisms of ultra-deep effective clastic reservoir and oil and gas exploration prospects. *Appl. Sci.* **2025**, *15*, 6984. [CrossRef]
26. Lu, S.K.; Bao, Z.H.; Yang, J.S. Structural deformation of the Lower-middle Jurassic series and their trap characteristics in Amu Darya right bank area. *Geoscience* **2013**, *27*, 774–782.
27. Nie, M.L.; Wu, L.; Liu, B.; Hou, L. Fault characteristic and reservoir-control effect in Amu Darya right bank area in Turkmenistan. *Xinjiang Pet. Geol.* **2013**, *34*, 365–368. (In Chinese)
28. Zhang, Y.; Li, C.; Li, J.; Luo, X.; Cheng, M.; Zhang, X.; Lu, B. A new method of geological modeling for the hydrocarbon secondary migration research. *Appl. Sci.* **2025**, *15*, 3377. [CrossRef]
29. Dou, M.; Li, S.; Lei, T.; Ren, G.; Li, X.; Guo, Y.; Feng, W.; Zhang, X. Hierarchical multiple-point geostatistical modeling method and application based on braided river reservoir architecture. *Minerals* **2022**, *12*, 1398. [CrossRef]
30. Liu, H.; Zhang, X.; Wang, Q. Quantitative prediction of braided sandbodies based on probability fusion and multi-point geostatistics. *Energies* **2023**, *16*, 2796. [CrossRef]
31. Wang, J.; He, Y.; Li, H.; Feng, B.; Zhao, Z.; Yu, X.; Hou, X. The genesis of a thin-bedded beach-bar system under the strike-slip extensional tectonic framework: A case study in the Bohai Bay Basin. *Appl. Sci.* **2025**, *15*, 7964.
32. Chen, G. Application of steerable pyramid decomposition technology in reservoir seismic prediction. *China Pet. Explor.* **2021**, *26*, 125–131.
33. Zhang, H.F.; Huang, X.R.; Zhang, J.; Ren, M. Strong seismic constraint modelling method based on steerable pyramid: A case study of fluvial facies in the second member of Shahejie Formation, Shengli Oilfield. *Oil Geophys. Prospect.* **2024**, *59*, 1197–1205. (In Chinese)

34. Huang, Z.-Y.; Gan, L.-D.; Dai, X.-F.; Li, L.-G.; Wang, J. Key parameter optimization and analysis of stochastic seismic inversion. *Appl. Geophys.* **2012**, *9*, 49–56. [CrossRef]
35. Franco, C.A.; Mukerji, T.; Mavko, G. Predicting reservoir petrophysical geobodies from seismic data using enhanced extended elastic impedance inversion. *Appl. Sci.* **2023**, *13*, 4755. [CrossRef]
36. Xu, Y.; Li, J.; Zhang, H. DFN modelling constrained by multiple seismic attributes using the steering pyramid technology. *Front. Earth Sci.* **2023**, *11*, 1257481. [CrossRef]
37. Abdi, Y.A.; Abdolghafour, M. A new robust weak supervision deep learning approach for reservoir properties prediction in Malaysian Basin field. *Appl. Sci.* **2023**, *13*, 9025. [CrossRef]
38. Pelemo-Daniels, D.; Stewart, R.R. Petrophysical property prediction from seismic inversion attributes using rock physics and machine learning: Volve field, North Sea. *Appl. Sci.* **2023**, *14*, 1345.
39. Zhao, A.; Yu, Y.; Wang, B.; Liu, Y.; Liu, J.; Fu, X.; Zheng, W.; Tian, F. Real-time intelligent recognition and precise drilling in strongly heterogeneous formations based on multi-parameter logging while drilling and drilling engineering. *Appl. Sci.* **2025**, *15*, 5536.
40. Zecchin, M.; Catuneanu, O.; Olariu, C. Reconstruction of land and marine features by seismic and surface geomorphology techniques. *Appl. Sci.* **2022**, *12*, 9611. [CrossRef]
41. Chen, Y.; Zhang, G. New parameters identification of proton exchange membrane fuel cell stacks based on an improved version of African vulture optimization algorithm. *Energy Rep.* **2022**, *8*, 3030–3040. [CrossRef]
42. Wang, E.; Xia, J.; Li, J.; Sun, X.; Li, H. Parameters exploration of SOFC for dynamic simulation using adaptive chaotic grey wolf optimization algorithm. *Energy* **2022**, *261*, 125146. [CrossRef]
43. Wang, H.; Zhao, L.; Peng, Q. An improved sand cat swarm optimization algorithm and its application to agricultural robot path planning. *Eng. Comput.* **2025**, *42*, 1525–1553. [CrossRef]
44. Dong, S.; Xia, Y.; Kamruzzaman, J. Quantum particle swarm optimization for task offloading in mobile edge computing. *IEEE Trans. Ind. Inform.* **2023**, *19*, 9113–9122.
45. Zhang, D.; Jiang, Z.; Mohammadzadeh, F.; Hasani Azhdari, S.M.; Abualigah, L.; Ghazal, T.M. FUZ-SMO: A fuzzy slime mould optimizer for mitigating false alarm rates in the classification of underwater datasets using deep convolutional neural networks. *Heliyon* **2024**, *10*, e28681. [CrossRef]
46. Liu, L.; Chu, C.; Chen, C.; Huang, S. MarineYOLO: Innovative deep learning method for small target detection in underwater environments. *Alex. Eng. J.* **2024**, *104*, 423–433. [CrossRef]
47. Yin, X.; Chen, L. Image object detection method based on improved Faster R-CNN. *J. Circuits Syst. Comput.* **2024**, *33*, 2450130.
48. Fan, J.; Yu, G.-A.; Zhao, M.; Zong, H. Addressing multi-scale temporal variability: Deep integration and application of the CNN and transformer model in monthly streamflow prediction. *Expert Syst. Appl.* **2025**, *292*, 128658. [CrossRef]
49. Naeem, H.; Dong, S.; Falana, O.; Ullah, F. Development of a deep stacked ensemble with process based volatile memory forensics for platform independent malware detection and classification. *Expert Syst. Appl.* **2023**, *223*, 119952. [CrossRef]
50. Zhang, C.; Guo, Z.; Li, C. Unsupervised anomaly detection for gearboxes based on the deep convolutional support generative adversarial network. *Sci. Rep.* **2025**, *15*, 8835. [CrossRef]
51. Cui, C.; Liu, L.; Qiao, R. A cutting-edge video anomaly detection method using image quality assessment and attention mechanism-based deep learning. *Alex. Eng. J.* **2024**, *108*, 476–485. [CrossRef]
52. Yu, L.; Zhang, D.; Liu, N.; Zhou, W. A multi-view fusion method via tensor learning and gradient descent for image features. *IEEE Access* **2021**, *9*, 79389–79399. [CrossRef]
53. Qian, D.; Yu, L.; Tang, H.; Zhao, J. Multiview feature fusion optimization method for image retrieval based on matrix correlation. *J. Electron. Imaging* **2020**, *29*, 053007. [CrossRef]
54. Yu, L.; Liu, P.; Jiang, L.; Zhao, Z. Tensor dispersion-based multi-view feature embedding for dimension reduction. *J. Electron. Imaging* **2021**, *30*, 033019.
55. Tian, C.; Chen, Y. Image segmentation and denoising algorithm based on partial differential equations. *IEEE Sens. J.* **2020**, *20*, 11935–11942.
56. Tian, C.; Zhang, H. Application of partial differential equation in brain image segmentation and registration. *IEEE Access* **2019**, *7*, 19631–19642. [CrossRef]
57. Yao, Y.; Xia, C.; Li, J.; Li, Q. Head CT image convolution feature segmentation and morphological filtering for densely matching points of IoTs. *IEEE Access* **2020**, *8*, 12521–12532. [CrossRef]
58. Wang, X.; Zhao, P.; Yue, S.; Gu, Y. An improved cross algorithm edge detection method and its application in coal gangue identification. *Int. J. Coal Prep. Util.* **2026**, *46*, 835–847.
59. Dong, S. Multi class SVM algorithm with active learning for network traffic classification. *Expert Syst. Appl.* **2021**, *176*, 114885. [CrossRef]

60. Wang, Y.; Feng, Y.; Sun, H. Research on vehicle intelligent wireless location algorithm based on convolutional neural network. *Neural Comput. Appl.* **2021**, *33*, 8131–8141.
61. Wang, W.; Dong, Q.; Hu, Z. Interactive piecewise planar building reconstruction from a single image based on geometric priors. *Expert Syst. Appl.* **2023**, *230*, 120572. [CrossRef]